






Cite this: *Nanoscale*, 2022, **14**, 2337

Improved polarization and endurance in ferroelectric $\text{Hf}_{0.5}\text{Zr}_{0.5}\text{O}_2$ films on $\text{SrTiO}_3(110)$ †

Tingfeng Song, Huan Tan, Saúl Estandía, Jaume Gàzquez,  Martí Gich, Nico Dix,  Ignasi Fina* and Florencio Sánchez  *

The metastable orthorhombic phase of $\text{Hf}_{0.5}\text{Zr}_{0.5}\text{O}_2$ (HZO) can be stabilized in thin films on $\text{La}_{0.67}\text{Sr}_{0.33}\text{MnO}_3$ (LSMO) buffered (001)-oriented SrTiO_3 (STO) by intriguing epitaxy that results in (111)-HZO oriented growth and robust ferroelectric properties. Here, we show that the orthorhombic phase can also be epitaxially stabilized on LSMO/STO(110), presenting the same out-of-plane (111) orientation but a different distribution of the in-plane crystalline domains. The remanent polarization of HZO films with a thickness of less than 7 nm on LSMO/STO(110) is $33 \mu\text{C cm}^{-2}$, which corresponds to a 50% improvement over equivalent films on LSMO/STO(001). Furthermore, HZO on LSMO/STO(110) presents higher endurance, switchable polarization is still observed up to 4×10^{10} cycles, and retention of more than 10 years. These results demonstrate that tuning the epitaxial growth of ferroelectric HfO_2 , here using STO(110) substrates, allows the improvement of functional properties of relevance for memory applications.

Received 21st October 2021,

Accepted 8th January 2022

DOI: 10.1039/d1nr06983g

rsc.li/nanoscale

1. Introduction

The discovery of a ferroelectric phase of HfO_2 ,¹ with robust properties at room temperature and compatibility with CMOS technology has renewed the interest of the industry in ferroelectric memories. The different properties of ferroelectric HfO_2 with respect to conventional ferroelectrics have raised fundamental questions and they may open up new applications. Ten years after the discovery of ferroelectric HfO_2 , these different properties are still far from being fully understood. They can depend to a great extent on point defects, parasitic phases, interfaces with electrodes and between grains, crystal orientation, and lattice strain. Unraveling the relative contribution of these factors to the ferroelectric properties is hampered by the complex microstructure of the doped HfO_2 films. Epitaxial films are more convenient than polycrystalline samples to advance towards this knowledge.^{2–7} Significant progress has recently been made by studying the epitaxial films of doped HfO_2 on $\text{La}_{0.67}\text{Sr}_{0.33}\text{MnO}_3$ (LSMO)

buffered (001)-oriented SrTiO_3 (STO) substrates. Relevant findings reported with epitaxial films include the demonstration of high polarization, endurance and retention in films of less than 5 nm thickness;⁸ proof of ferroelastic domain switching;⁹ demonstration of thickness (t) dependence on the coercive electric field (E_c) according to $E_c - t^{-2/3}$ scaling;^{8,10–12} estimation of the Curie temperature by X-ray diffraction measurements;¹³ control of the relative amount of ferroelectric and paraelectric phases by substrate selection;¹⁴ and improvement of endurance in the presence of a parasitic monoclinic phase.¹⁵

Epitaxial growth can facilitate the strain control of functional properties. This is demonstrated for perovskite ferroelectrics on perovskite substrates,^{16,17} but the epitaxial growth of fluorite ferroelectrics on perovskite substrates is much less flexible. Probably because of the large structural difference between HfO_2 and perovskite substrates, epitaxy occurs by the so-called domain matching epitaxy mechanism,¹⁸ which results in a non-significant change of the lattice parameters of HfO_2 by changing the lattice mismatch *via* appropriate substrate selection.^{10,14} Furthermore, the orthorhombic phase grows epitaxially on LSMO and other La-doped manganites, but not on other popular oxide electrodes such as SrRuO_3 , LaNiO_3 or La:BaSnO_3 .¹⁹ These facts limit the possibilities of controlling the microstructure and the ferroelectric properties of epitaxial HfO_2 films. Aiming to open new ways of control, we have investigated the growth of $\text{Hf}_{0.5}\text{Zr}_{0.5}\text{O}_2$ (HZO) films on STO(110) substrates buffered with LSMO electrodes. The films are epitaxial and (111) oriented like equivalent films on STO

Institut de Ciència de Materials de Barcelona (ICMAB-CSIC), Campus UAB, Bellaterra 08193, Barcelona, Spain. E-mail: ifina@icmab.es, jsanchez@icmab.es

† Electronic supplementary information (ESI) available: Simulation of Laue oscillations. Piezoresponse force microscopy amplitude images. Sketches of the epitaxial relationships between crystal variants and substrates. STEM: simultaneous ABF and HAADF images. Top view of HZO(111) on LSMO(110). STEM characterization (reconstructed image from reflections in the Fourier space). Atomic force microscopy image of the HZO/LSMO/STO(110) sample. Leakage curves during endurance tests. Polarization loops during endurance tests. See DOI: 10.1039/d1nr06983g



(001), but they present a different set of in-plane crystal variants. We observe that this different crystalline microstructure has an impact on functional properties, *i.e.* ferroelectric polarization is very high around $33 \mu\text{C cm}^{-2}$ in films of less than 7 nm thickness, representing an increase of 50% over equivalent films on STO(001). Films grown on STO(110) can be cycled with reduced electrical strength because of the higher polarization, which allows the enhancement of the endurance up to 4×10^{10} cycles.

2. Experimental

HZO films were grown on LSMO buffered STO(001) and STO(110) substrates by pulsed laser deposition (PLD) using a KrF excimer laser. HZO films ($t = 6.5 \text{ nm}$) and LSMO electrodes ($t = 25 \text{ nm}$) were grown in a single process. HZO was deposited under optimal growth conditions: a laser frequency of 2 Hz, a dynamic oxygen pressure of 0.1 mbar, and a substrate temperature (heater block temperature) of 800°C .^{10,20} Films were cooled at the end of deposition under 0.2 mbar oxygen pressure. Platinum circular top electrodes of $20 \mu\text{m}$ diameter and 20 nm thickness, were placed *ex situ* at room temperature by sputtering through stencil masks.

Crystal phase identification and epitaxy characterization were performed by X-ray diffraction (XRD) with Cu K α radiation using a Siemens D5000 diffractometer equipped with a point detector, and a Bruker D8-Advance diffractometer equipped with a 2D detector. Microstructural characterization was performed by scanning transmission electron microscopy using a JEOL ARM 200CF STEM with a cold field emission source, equipped with a CEOS aberration corrector and operated at 200 kV. Film topography was analyzed using atomic force microscopy (AFM) using a Keysight 5100 analyzer. Ferroelectric characterization was carried out using an AixACCT TFAAnalyser2000 platform. Polarization loops were measured at 1 kHz by the dynamic leakage current compensation (DLCC)²¹ procedure at room temperature in top-bottom configuration, with the bottom LSMO electrode grounded. Residual leakage and series resistance contributions were subtracted using the reported methodology.²² Endurance was measured at room temperature by cycling the sample at a frequency of 100 kHz using bipolar square pulses of indicated amplitude and measuring polarization loops at 1 kHz. Retention was measured at 85°C , poling the sample with a triangular pulse of 0.25 ms and determining the remanent polarization from the first polarization curve of the polarization loop measured at 1 kHz using the positive up-negative down protocol after a delay time. Piezoelectric force microscopy (PFM) measurements were performed with an MFP-3D microscope (Oxford Instrument Co.) using the BudgetSensors silicon (n-type) cantilevers with the Pt coating (Multi75E-G). To achieve better sensitivity, the dual AC resonance tracking (DART) method was employed.²³ PFM voltage hysteresis loops were always performed at remanence at a dwell time of 100 ms. Due to the difficulties in quantifying PFM response in

DART, piezoelectric coefficients have not been evaluated, but all the measurements in the characterized samples were performed under the same conditions, making them comparable.

3. Results

Fig. 1a shows the XRD θ - 2θ scans of HZO/LSMO films on STO(001) (black line) and STO(110) (red line). The highest intensity peaks are STO reflections, and the shoulders on the right of these peaks are the corresponding LSMO reflections (LSMO grows with a cube-on-cube epitaxial relationship on STO). The HZO film on LSMO/STO(001) shows an orthorhombic (*o*) *o*-HZO(111) peak at $2\theta \sim 30^\circ$. A longer time scan around this peak is shown in Fig. 1b. The low intensity peaks on both sides of the *o*-HZO(111) reflection are Laue oscillations. The thickness of the film, according to the simulation of the peak and Laue fringes (Fig. S1, ESI†) is 6.5 nm, and the *o*-HZO(111) spacing is $d_{o\text{-HZO}(111)} = 2.972 \text{ \AA}$, matching well with the values reported for equivalent films.¹⁰ The scan of the film on LSMO/STO(110) presents an intense *o*-HZO(111) peak and the absence of peaks corresponds to other orientations of the orthorhombic phase or other polymorphs. The *o*-HZO(111) peak is accompanied by Laue fringes (see the simulation in Fig. S1, ESI†). The thickness is 6.5 nm, and the out-of-plane

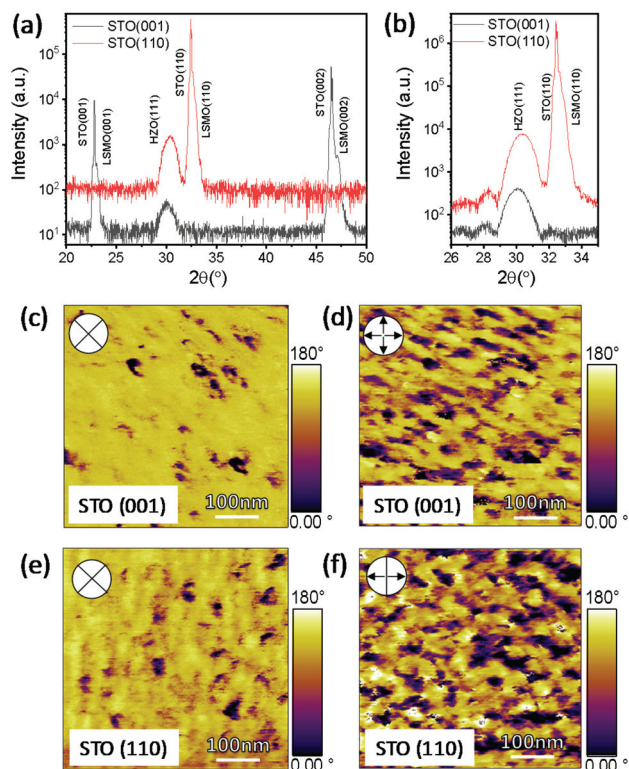


Fig. 1 (a) XRD θ - 2θ scan of HZO/LSMO/STO(001) (black line) and HZO/LSMO/STO(110) (red line) samples. (b) Zoomed scans, recorded with longer time, around the *o*-HZO(111) reflection. (c) Vertical and (d) in-plane phase contrasts for HZO/LSMO/STO(001). (e) Vertical and (f) in-plane phase contrasts for HZO/LSMO/STO(110).



interplanar spacing $d_{o\text{-HZO}(111)} = 2.946 \text{ \AA}$ is slightly lower than that of the film on STO(001). For the film grown on LSMO/STO(001), the vertical and in-plane PFM images show a predominant downward polarization direction with a mixture of in-plane polarization along opposite directions (Fig. 1d) in the as-grown state. Note that the lateral PFM shows a maximum response when the cantilever lies perpendicular to the polar axis of the film.²⁴ The film grown on LSMO/STO(110) shows similar vertical and in-plane contrasts (Fig. 1d and e). The corresponding amplitude images of Fig. 1c–f are shown in Fig. S2, ESI†. These results are in agreement with the tilted polarization along the [001] direction diagonal to the (111) texture of the films. It can be also disregarded as an important contribution of any (001) texture in the films.

Epitaxy has been studied by XRD using a 2D detector. Fig. 2a shows the reciprocal space map (RSM) around the asymmetric STO{111} reflections for the HZO/LSMO/STO(001) sample. The map was obtained from ϕ -scans with a 2D detector, recorded at ϕ angles ranging from 0° to 360° , with a step $\Delta\phi = 1^\circ$. In addition to the STO{111} spot, the integrated frame shows the presence of a spot that corresponds to $o\text{-HZO}\{11\bar{1}\}$ reflections ($Q_x = 0.316 \text{ \AA}^{-1}$, $Q_z = 0.109 \text{ \AA}^{-1}$) and a lower intensity spot of $o\text{-HZO}\{200\}$ reflections ($Q_x = 0.316 \text{ \AA}^{-1}$, $Q_z = 0.224 \text{ \AA}^{-1}$). The presence of both spots at the same ϕ is due to 180° twinning. The diffraction spots appear at specific ϕ angles, as can be seen in Fig. 2b. Fig. 2b shows a $Q_z - \phi$ map obtained by slicing the RSM around $Q_x = 0.316 \text{ \AA}^{-1}$ ($\Delta Q = \pm 0.01 \text{ \AA}^{-1}$). The integrated region corresponds to the region enclosed by a dashed rectangle in Fig. 2a. There are 12 spots, 30° apart, corresponding to both $o\text{-HZO}\{11\bar{1}\}$ and $o\text{-HZO}\{200\}$ reflections. The pole figure of $o\text{-HZO}\{11\bar{1}\}$ reflections

shown in Fig. 2c allows us to visualize more clearly the presence of four families of in-plane crystal variant consequences of the epitaxy of $o\text{-HZO}(111)$ (3-fold symmetry surface) on LSMO/STO(001) (4-fold symmetry surface).¹⁸ The four families are indicated by colored triangles. Similar measurements for the HZO/LSMO/STO(110) sample are presented in Fig. 2d–f. Fig. 2d shows the RSM around the asymmetric STO{011} reflections. In addition to the substrate spot, there are $o\text{-HZO}\{11\bar{1}\}$ ($Q_x = 0.313 \text{ \AA}^{-1}$, $Q_z = 0.115 \text{ \AA}^{-1}$) and $o\text{-HZO}\{200\}$ reflections ($Q_x = 0.313 \text{ \AA}^{-1}$, $Q_z = 0.225 \text{ \AA}^{-1}$). The $Q_z - \phi$ map (Fig. 2e) shows 12 $o\text{-HZO}\{11\bar{1}\}$ and 12 $o\text{-HZO}\{200\}$ spots. The 12 spots are distributed in 6 sets of 2 spots, each set is about 60° apart and the two spots in each set are 8.5° apart. Other heterostructures with complex domain structures have shown similar sets of peaks in ϕ -scans.^{25,26} The pole figure shown in Fig. 2f proves the angular distribution of $o\text{-HZO}\{11\bar{1}\}$ reflections. The pole figure indicates that there are four HZO crystal domains (Fig. S3, ESI†), corresponding to the following epitaxial relationships: $[-211]\text{HZO}(111)/[-112]\text{STO}(110)$, $[-211]\text{HZO}(111)/[1\bar{1}2]\text{STO}(110)$, $[2\bar{1}1]\text{HZO}(111)/[-112]\text{STO}(110)$, and $[2\bar{1}1]\text{HZO}(111)/[1\bar{1}2]\text{STO}(110)$.

To better understand the epitaxy, we have conducted cross-sectional STEM characterization along the [001] zone axis of STO. Fig. 3a shows an inverse-intensity annular bright field (ABF) image where the HZO and LSMO layers and the STO substrate are visualized (horizontal yellow arrows mark the position of the interfaces). The original ABF image and simultaneously acquired high-angle annular dark field images are shown in Fig. S4, ESI†. Fig. 3a shows that HZO is orthorhombic, and different crystal variants were observed (vertical yellow arrows mark the position of boundaries between var-

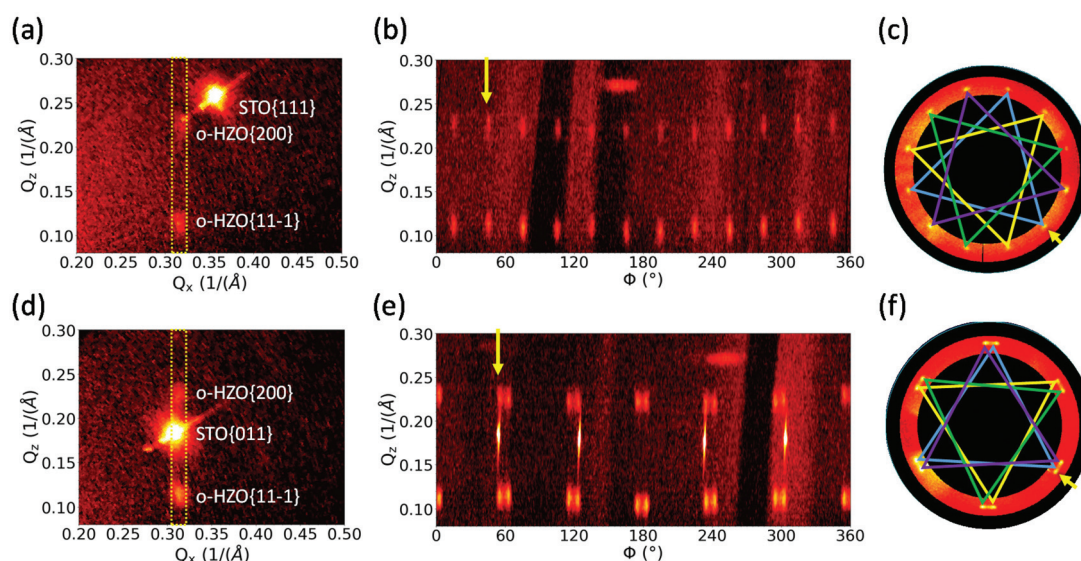


Fig. 2 (a and d) RSM obtained from processing 2D pole figure frames. Q_z is the perpendicular component and Q_x is parallel to the in-plane direction at a specific ϕ angle. The dashed rectangle indicates the integrated Q_x range in the $Q_z - \phi$ map plotted in (b and e). The yellow arrows indicate the ϕ position of RSM in (a and d). (c and f) Pole figures corresponding to the $o\text{-}\{11\bar{1}\}$ planes integrated around $\chi = 71 \pm 7^\circ$ and $2\theta = 27\text{--}33^\circ$. The triangles are the guides to the eyes to indicate the four crystallographic $o\text{-}\{111\}$ domains. Panels (a–c) and (d–f) correspond to the measurements of HZO/LSMO/STO(001) and HZO/LSMO/STO(110), respectively.



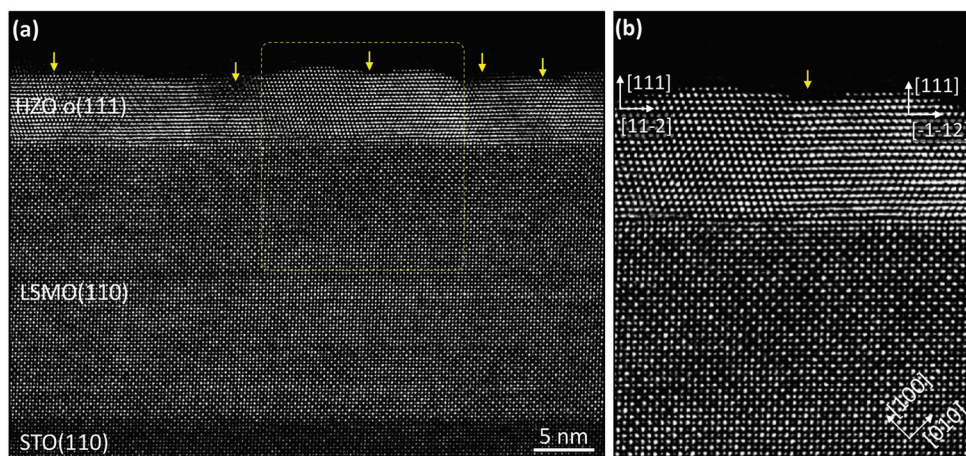


Fig. 3 (a) Cross-sectional contrast inverted annular bright field image showing, from bottom to top, the STO(110) substrate, the LSMO(110) electrode and the HZO(111) film. The locations of the (coherent) boundaries between mirror-like in-plane crystallographic variants are indicated by yellow arrows at the top of the image. (b) Zoomed region showing two orthorhombic HZO grains and part of the LSMO electrode. (b) has been extracted from within the area marked with the yellow dashed line in (a).

iants). There is absence of the monoclinic phase or other HZO polymorphs in Fig. 3a, although monoclinic grains were occasionally observed in other regions of the STEM specimen. Thus, the HZO film on LSMO/STO(110) is almost purely orthorhombic. This is remarkable since equivalent films on LSMO/STO(001) show the coexistence of orthorhombic and monoclinic phases.¹⁴ The rectangular area marked with a dashed yellow line is shown in an enlarged view in Fig. 3b. This image confirms the high crystalline quality of HZO and shows a well-defined (semi) coherent HZO/LSMO interface. The lattice mismatch, around -11% , is too high for conventional epitaxy. Indeed, the comparison of LSMO(110) and HZO(111) unit cells does not reveal direct matching (Fig. S5, ESI†). Domain matching epitaxy recently observed in the high-mismatch growth of HZO on LSMO(001),¹⁸ is also expected to occur in films grown on LSMO(110). To confirm this, we obtained reconstructed STEM images by filtering in the Fourier space (Fig. S6, ESI†). The analysis confirms the presence of extra planes at the HZO/LSMO interface with the periodicity anticipated in domain matching epitaxy. Finally, we note that HZO is (111) oriented on both LSMO(001) and LSMO(110) surfaces. This suggests the relevance of the surface energy contribution in addition to the interface energy. On the other hand, atomic force microscopy measurements confirm that the film on STO(110) is very flat, with a root mean square roughness of 0.25 nm (Fig. S7, ESI†), which is comparable to the films on STO(001).¹⁰

The measurements of polarization loops confirm that the HZO films on LSMO/STO(001) and LSMO/STO(110) are ferroelectric (Fig. 4). The current–voltage curve (black line) of the film on STO(001) shows two ferroelectric switching peaks at -2.7 and $+1.8\text{ V}$. The average coercive field (E_C) is $E_C = 3.4\text{ MV cm}^{-1}$ and there is an internal field of 1.3 MV cm^{-1} , pointing from the upper Pt contact towards the lower LSMO electrode, as shown by PFM characterization. The polarization loop (Fig. 3b, black line) is well saturated and the remanent polariz-

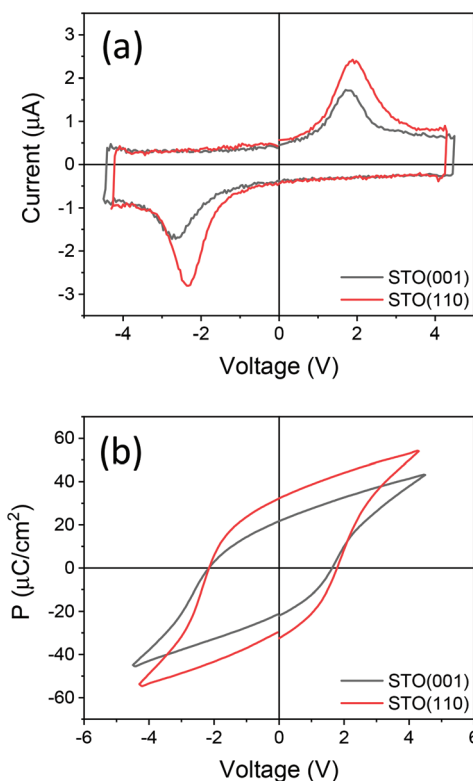


Fig. 4 (a) Current–voltage curves of HZO/LSMO/STO(001) (black line) and HZO/LSMO/STO(110) (red line) samples, measured in the pristine state. (b) Corresponding polarization loops.

ation (P_r) is $22\text{ }\mu\text{C cm}^{-2}$, similar to the reported values for films of comparable thickness.¹⁰ Fig. 3 also shows the current–voltage curve and the polarization loop of the equivalent film on LSMO/STO(110) (red lines). In this sample, the coercive voltages are -2.3 and $+1.9\text{ V}$, corresponding to an average E_C of



3.4 MV cm⁻¹ and an internal field of 0.6 MV cm⁻¹. The remanent polarization, $P_r = 33 \mu\text{C cm}^{-2}$, is much higher than the usual values reported for HZO.^{2,3} Remarkably, P_r is 50% higher than the equivalent epitaxial film grown simultaneously on STO(001). The larger polarization is likely the consequence of the higher amount of the orthorhombic phase in the film on LSMO/STO(110). STEM characterization showed that it is almost purely orthorhombic (Fig. 3), while films on LSMO/STO(001) present an important amount of the parasitic monoclinic phase.¹⁴ Theoretical calculations predicted a spontaneous polarization of 52–55 $\mu\text{C cm}^{-2}$ for orthorhombic HfO₂.^{27,28} The projected polarization along the [111] direction of a pure orthorhombic phase film would be around 31 $\mu\text{C cm}^{-2}$, which is similar to the measured remanent polarization. On the other hand, the HZO film on STO(110) presents a leakage current of about $5 \times 10^{-7} \text{ A cm}^{-2}$ at 1 MV cm⁻¹, less than about $1 \times 10^{-6} \text{ A cm}^{-2}$ of the film on STO(001) (Fig. S8, ESI†).

Fig. 5 shows the endurance measurements of the films. The film on STO(001) (Fig. 5a) was cycled with sub-coercive field voltage pulses of 3.5 V (electric field $E = 5.4 \text{ MV cm}^{-1}$) having $2P_r = 24.2 \mu\text{C cm}^{-2}$ in the pristine state (solid blue circles). Wake-up effect is not observed. Polarization does not change significantly after 10^5 cycles, but additional cycles cause fatigue. The measurements were stopped when the polarization was as low as $2P_r = 3.3 \mu\text{C cm}^{-2}$ after 4×10^9 cycles. The current leakage (open blue circles in Fig. 5a) was constant up to 10^7 cycles and increased dramatically with additional cycles (see current–voltage curves in Fig. S8, ESI†). The test of endurance at 3 V (solid green diamonds) shows a similar dependence. The polarization in the pristine state is lower, but the fatigue after 10^5 cycles is less pronounced and the capacitor was cycled up to 10^{10} cycles (the test was stopped due to the low $2P_r$ at $3 \mu\text{C cm}^{-2}$, see polarization–voltage loops shown in Fig. S9, ESI†). The current leakage (open green diamonds in Fig. 5a) was constant during the test. The film on STO(110), switched at the same voltage of 3.5 V (Fig. 5b, solid black squares), has a larger initial polarization, $2P_r = 47 \mu\text{C cm}^{-2}$. It presents slight fatigue from the first cycles, being more pronounced after 10^5 cycles, and there was a breakdown after $2 \times$

10^9 cycles. The breakdown is likely due to the increased leakage after cycling (open black squares), which was larger than in the sample grown on STO(110) after 10^9 cycles. Reducing the electric field is essential to avoid the breakdown. The remanent polarization of the film on STO(110) is very high, and by applying a lower voltage of 3 V ($E = 4.6 \text{ MV cm}^{-1}$), the initial polarization, $2P_r = 30 \mu\text{C cm}^{-2}$, is greater than in the film on STO(001) cycled with 3.5 V pulses. The evolution of polarization with cycling (solid red triangles in Fig. 5b) is similar to that at a higher field, but in this case, there is no electrical breakdown up to 4×10^{10} cycles when $2P_r$ decreased to $4 \mu\text{C cm}^{-2}$ and the measurement was stopped. Polarization fatigue is the main factor that limits endurance in epitaxial HZO films. The robustness against breakdown is probably because of the fact that the current leakage (open red triangles in Fig. 5b), contrary to what was observed for the 3.5 V cycling voltage, does not increase significantly during cycling.

Fig. 6 shows the retention measurements of the HZO/LSMO/STO(110) sample, after poling a capacitor with pulses of amplitudes +3 V (solid triangles) and –3 V (open triangles). The measurements were performed at a temperature of 85 °C.

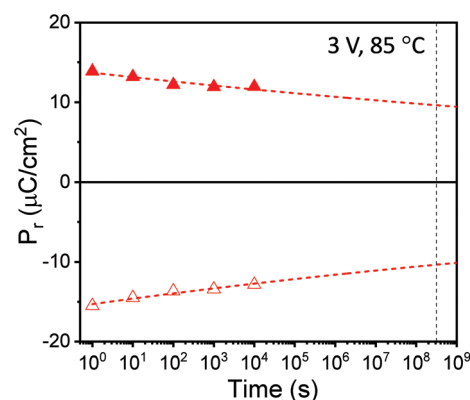


Fig. 6 Polarization retention measurements at 85 °C of HZO/LSMO/STO(110) for the positive and negative poling of 3 V. Lines are fits to $P_r = P_0 \tau_d^n$ equation.

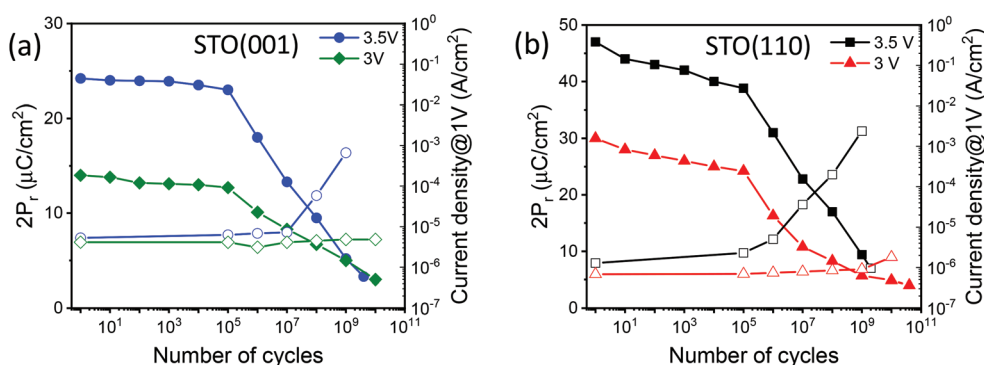


Fig. 5 (a) Endurance (solid symbols) and current leakage as a function of the number of cycles (empty symbols) of the HZO/LSMO/STO(001) sample cycled at 3.5 V (blue symbols) and 3 V (green symbols). (b) Endurance (solid symbols) and current leakage as a function of the number of cycles (empty symbols) of the HZO/LSMO/STO(110) sample cycled at 3.5 V (black symbols) and 3 V (red symbols).



Dashed red lines are fits to $P_r = P_0 \cdot \tau_d^n$ equation, where τ_d is the delay time and n a fitting parameter.²⁹ The vertical black dashed line indicates a time of 10 years. The extrapolated polarization is high after 10 years for both positive and negative poling at 3 V, the poling amplitude that allows an endurance of 4×10^{10} cycles. Therefore, the film shows high polarization ($2P_r = 30 \mu\text{C cm}^{-2}$), endurance (4×10^{10} cycles) and retention (more than 10 years) under the same poling voltage.

4. Conclusions

In summary, it is shown that the epitaxial stabilization of the orthorhombic phase of HZO on LSMO/STO(001) also occurs on LSMO/STO(110). HZO films are (111) oriented and have in-plane crystal variants on both substrates, but the variants have different angular distributions. The use of an STO(110) substrate allows the increase of ferroelectric polarization by 50%, with a high remanent polarization of $33 \mu\text{C cm}^{-2}$ in a film of less than 7 nm thickness. The high polarization is accompanied by very large endurance (4×10^{10} cycles) and retention extrapolated to more than 10 years. The results point out that adjusting the epitaxial growth, here carried out by the orientation of the substrate, can allow further improvements of the properties.

Conflicts of interest

There are no conflicts to declare.

Acknowledgements

Financial support from the Spanish Ministry of Science and Innovation, through the Severo Ochoa FUNFUTURE (CEX2019-000917-SMCIN, AEI/10.13039/501100011033), PID2020-112548RB-I00 (MCIN/AEI/10.13039/501100011033) and PID2019-107727RB-I00 (MCIN/AEI/10.13039/501100011033) projects, from CSIC through the i-LINK (LINKA20338) program, and from Generalitat de Catalunya (2017 SGR 1377) is acknowledged. The project is supported by a 2020 Leonardo Grant for Researchers and Cultural Creators, BBVA Foundation. IF acknowledges Ramón y Cajal contract RYC-2017-22531. TS and HT are financially supported by China Scholarship Council (CSC) with No. 201807000104 and 201906050014. TS and HT works have been done as a part of their Ph.D. program in Materials Science at Universitat Autònoma de Barcelona.

References

- 1 T. S. Böske, J. Müller, D. Bräuhäus, U. Schröder and U. Böttger, *Appl. Phys. Lett.*, 2011, **99**, 102903.
- 2 I. Fina and F. Sánchez, *ACS Appl. Electron. Mater.*, 2021, **3**, 1530.
- 3 J. Cao, S. Shi, Y. Zhu and J. Chen, *Phys. Status Solidi RRL*, 2021, **15**, 2100025.
- 4 T. Shimizu, K. Katayama, T. Kiguchi, A. Akama, T. J. Konno, O. Sakata and H. Funakubo, *Sci. Rep.*, 2016, **6**, 32931.
- 5 J. Lyu, I. Fina, R. Solanas, J. Fontcuberta and F. Sánchez, *Appl. Phys. Lett.*, 2018, **113**, 082902.
- 6 Y. Wei, P. Nukala, M. Salverda, S. Matzen, H. J. Zhao, J. Momand, A. S. Everhardt, G. Agnus, G. R. Blake, P. Lecoeur, B. J. Kooi, J. Íñiguez, B. Dkhil and B. Noheda, *Nat. Mater.*, 2018, **17**, 1095.
- 7 Z. Zhang, S. Hsu, V. A. Stoica, H. Paik, E. Parsonnet, A. Qualls, J. Wang, L. Xie, M. Kumari, S. Das, Z. Leng, M. McBriarty, R. Proksch, A. Gruverman, D. G. Schlom, L. Chen, S. Salahuddin, L. W. Martin and R. Ramesh, *Adv. Mater.*, 2021, **33**, 2006089.
- 8 J. Lyu, T. Song, I. Fina and F. Sánchez, *Nanoscale*, 2020, **12**, 11280.
- 9 T. Shimizu, T. Mimura, T. Kiguchi, T. Shiraishi, T. Konno, Y. Katsuya, O. Sakata and H. Funakubo, *Appl. Phys. Lett.*, 2018, **113**, 212901.
- 10 J. Lyu, I. Fina, R. Solanas, J. Fontcuberta and F. Sánchez, *ACS Appl. Electron. Mater.*, 2019, **1**, 220.
- 11 T. Song, R. Bachelet, G. Saint-Girons, R. Solanas, I. Fina and F. Sánchez, *ACS Appl. Electron. Mater.*, 2020, **2**, 3221.
- 12 T. Song, R. Bachelet, G. Saint-Girons, N. Dix, I. Fina and F. Sánchez, *J. Mater. Chem. C*, 2021, **9**, 12224.
- 13 T. Mimura, T. Shimizu, Y. Katsuya, O. Sakata and H. Funakubo, *Jpn. J. Appl. Phys.*, 2020, **59**, SGGB04.
- 14 S. Estandía, N. Dix, J. Gazquez, I. Fina, J. Lyu, M. F. Chisholm, J. Fontcuberta and F. Sánchez, *ACS Appl. Electron. Mater.*, 2019, **1**, 1449.
- 15 T. Song, S. Estandía, H. Tan, N. Dix, J. Gázquez, I. Fina and F. Sánchez, *Adv. Electron. Mater.*, 2021, 2100420.
- 16 D. G. Schlom, L. Q. Chen, C. B. Eom, K. M. Rabe, S. K. Streiffer and J. M. Triscone, *Annu. Rev. Mater. Res.*, 2007, **37**, 589.
- 17 L. W. Martin and A. M. Rappe, *Nat. Rev. Mater.*, 2017, **2**, 16087.
- 18 S. Estandía, N. Dix, M. F. Chisholm, I. Fina and F. Sánchez, *Cryst. Growth Des.*, 2020, **20**, 3801.
- 19 S. Estandía, J. Gázquez, M. Varela, N. Dix, M. Qian, R. Solanas, I. Fina and F. Sánchez, *J. Mater. Chem. C*, 2021, **9**, 3486.
- 20 J. Lyu, I. Fina and F. Sánchez, *Appl. Phys. Lett.*, 2020, **117**, 072901.
- 21 R. Meyer, R. Waser, K. Prume, T. Schmitz and S. Tiedke, *Appl. Phys. Lett.*, 2005, **86**, 142907.
- 22 S. González-Casal, I. Fina, F. Sánchez and J. Fontcuberta, *ACS Appl. Electron. Mater.*, 2019, **1**, 1937.
- 23 B. J. Rodriguez, C. Callahan, S. V. Kalinin and R. Proksch, *Nanotechnology*, 2007, **18**, 475504.
- 24 E. Gradauskaitė, N. Gray, M. Campanini, M. D. Rossell and M. Trassin, *Chem. Mater.*, 2021, **33**, 9439.
- 25 H. N. Lee, D. Hesse, N. Zakharov and U. Gösele, *Science*, 2002, **296**, 2006.



- 26 J. Roldán, F. Sánchez, V. Trtik, C. Guerrero, F. Benitez, C. Ferrater and M. Varela, *Appl. Surf. Sci.*, 2000, **154**–**155**, 159.
- 27 T. D. Huan, V. Sharma, G. A. Rossetti and R. Ramprasad, *Phys. Rev. B: Condens. Matter Mater. Phys.*, 2014, **90**, 064111.
- 28 F. Delodovici, P. Barone and S. Picozzi, *Phys. Rev. Mater.*, 2021, **5**, 064405.
- 29 D. J. Kim, J. Y. Jo, Y. S. Kim, Y. J. Chang, J. S. Lee, J.-G. Yoon, T. K. Song and T. W. Noh, *Phys. Rev. Lett.*, 2005, **95**, 237602.

